Tuning Spin Transport in a Graphene Antiferromagnetic Insulator

Petr Stepanov[1,2,*] Dmitry L. Shcherbakov,[1] Shi Che,[1] Marc W. Bockrath,[1] Yafis Barlas,[3]
Dmitry Smirnov,[4] Kenji Watanabe,[5] Takashi Taniguchi,[6] Roger K. Lake,[7] and Chun Ning Lau[1,†]

[1]*Department of Physics, The Ohio State University, Columbus, Ohio 43221, USA*

[2]*ICFO - Institut de Ciencies Fotoniques, The Barcelona Institute of Science and Technology, Castelldefels, Barcelona 08860, Spain*

[3]*Department of Physics, University of Nevada, Reno, Nevada 89557, USA*

[4]*National High Magnetic Field Laboratory, Tallahassee, Florida 32310, USA*

[5]*Research Center for Functional Materials, National Institute for Materials Science, 1-1 Namiki, Tsukuba, 305-0044 Japan*

[6]*International Center for Materials Nanoarchitectonics, National Institute for Materials Science, 1-1 Namiki, Tsukuba 305-0044, Japan*

[7]*Department of Electrical and Computer Engineering, University of California, Riverside, Riverside, California 92521, USA*

Long-distance spin transport through antiferromagnetic insulators (AFMIs) is a long-standing goal of spintronics research. Unlike conventional spintronics systems, monolayer graphene in the quantum Hall regime (QH) offers an unprecedented tuneability of spin-polarization and charge-carrier density in QH edge states. Here, using gate-controlled QH edges as spin-dependent injectors and detectors in an all-graphene electrical circuit, we demonstrate a selective tuning of ambipolar spin transport through graphene $\nu = 0$ AFMIs. By modulating polarities of the excitation bias, magnetic fields, and charge carriers that host opposite chiralities, we show that the difference between spin chemical potentials of adjacent edge channels in the spin-injector region is crucial in tuning spin transport observed across graphene AFMI. We demonstrate that nonlocal response vanishes upon reversing directions of the co-propagating edge channels when the spin filters in our devices are no longer selective for a particular spin polarization. Our results establish a versatile set of methods to tune pure spin transport via an antiferromagnetic media and open a pathway to explore their applications for a broad field of antiferromagnetic spintronics research.

I. INTRODUCTION

Achieving long-distance ($\gg 10$ nm) dissipationless spin transport and understanding its microscopic mechanism are worthwhile goals of antiferromagnetic spintronics research [1–3]. A plethora of condensed-matter systems has been recently proposed as active components of ferromagnetic spin-transport devices [4–8]. For example, in magnetically doped insulators spin currents can be carried via magnon quasiparticles [9,10], while in easy-plane magnetically ordered systems, spin currents can be carried via dissipationless mechanisms, such as spin superfluidity [1,2,11–15]. Recently, monolayer graphene (MLG) in the quantum Hall regime (QH) has been realized as a highly tunable system for spintronic studies [16–19].

High magnetic field frequently breaks an approximate SU(4) symmetry of MLG, giving rise to a set of symmetry-broken Landau levels (LLs) with integer fillings $\nu = \pm 2$, ± 1 and 0 [20–33]. While states at fully filled or fully emptied zeroth Landau level ($\nu = +2$ and $\nu = -2$, respectively) host two co-propagating edge channels with opposite spin order, QH states at $\nu = \pm 1$ are spontaneously oppositely spin polarized [21,24,26,34]. The half-filled ($\nu = 0$) zeroth LL is a unique QH state and is now broadly recognized by theoretical and experimental research [20,21] that in the vicinity of high magnetic fields its ground state is a canted antiferromagnet (CAF), where charge quasiparticles occupy graphene's two sublattices with almost oppositely directed spins in an easy-plane configuration.

II. DETECTING SPIN-CURRENT USING CHIRAL QH EDGE STATES

Because of the small spin-orbit coupling and extremely small spin-anisotropy, QH states in graphene have been

*petr.stepanov@icfo.eu
†lau232@osu.edu

proposed as a platform for spintronics research [11,35]. In contrast to conventional spintronics systems [1,9], graphene offers a remarkable *in situ* tunability of charge-carrier density and spin-polarization in QH edge channels, when charge carriers' Fermi level can be capacitively tuned by changing the electrostatic potential on the back-gate electrode. By tuning the external fields, we demonstrate how chiral QH edge states switch the spin-transport polarity. We utilize QH states within zeroth LL to detect a large nonlocal response V_{nl}. V_{nl} is asymmetric upon reversing the bias polarity, which originates from different hotspots generated by interchannel scattering and may likely be explained by spin-canting direction in the CAF state. When the direction of the out-of-plane magnetic field is reversed, we observe a complete quenching of the nonlocal response, pointing towards a spin-filtering mechanism shut-off on both sides of the CAF state and explained by the reversed direction of the edge channel propagation. Lastly, we demonstrate the revival of the nonlocal signal using holelike QH states in the same device.

Figure 1(a) illustrates schematics of QH states in a long (approximately 15 μm) *h*-BN-encapsulated graphene channel. On top of each sample we fabricate three metal top gates following the geometry proposed in Ref. [11] and experimentally realized in previous works [16,17] [insets in Fig. 1(a)]. Devices in this study are fabricated using a dry-transfer technique. First, we use a thin polypropylene carbonate (PPC) layer placed on top of the polydimethyl-siloxane (PDMS) stamp to pick up a top *h*-BN layer of a few tens of nanometers thick at 40 °C. Next we pick up a graphene flake mechanically exfoliated on a SiO$_2$/Si^{++} wafer, followed by the subsequent pick up of the bottom *h*-BN flake, which fully encapsulates graphene between clean atomically flat *h*-BN interfaces. In the last step, the stacks are placed on the target SiO$_2$/Si^{++} substrate followed by the release of the PPC layer from the PDMS stamp at 90 °C. The next step of fabrication consists of etching the stack into a multiple Hall-bar geometry using reactive plasma etching by a high-power SF$_6$ plasma. Next, we couple the graphene sheet to the Cr/Au metallic contacts (10/50 nm). At the last step, Cr/Au metallic top gates are deposited on top of the sample separated by a thin Al$_2$O$_3$ layer deposited beforehand to exclude short-ages of the top gates with the graphene channel. At the end of the nanofabrication process, we obtain a graphene sample with 15 leads for proper transport characterization, three top gates and one bottom gate to independently control charge-carrier densities in four regions of the graphene channel.

We apply voltage to the Si back gate so the non-top-gated regions [blue regions in Fig. 1(a)] host QH states at fillings $\nu = \pm 2$. The central top gate tunes the Fermi level into the charge neutrality point with $\nu = 0$. Left and right top gates serve as spin filters in the spin-injection (red box $\nu = +2/+1/+2$) and spin-detection (blue box

$\nu = +2/+1/+2$) regions, respectively. Spin selectivity is defined by the QH state in the side-top-gated regions. A bias voltage is applied between the inner and outer $\nu = 2$ sections in the injection region, while a nonlocal voltage V_{nl} is measured between the inner and outer $\nu = 2$ sections in the detection region.

In this experiment, edge-state configurations play a crucial role in controlling the spin-current injection and detection processes. Figure 1(b) shows QH states inside the spin-injector and spin-detector regions. When bias is applied between the $\nu = 2$ sections in the injection region, the high-energy ("hot") carriers propagate from source to drain electrode (marked **S** and **D**, respectively); at the corner of the spin-filtering $\nu = +1$ QH state (pink circle), only the ↑-spin-polarized (red) channel of the outer $\nu = +2$ QH state is permitted into the $\nu = +1$ QH-state region without loss of momenta, thus undergoing the spin-filtering process. The yellow circle indicates another pivot point, where the previously selected ↑-spin-polarized (red) channel enters the inner $\nu = +2$ QH state further generating a spin-angular-momentum imbalance between adjacent co-propagating edge channels. The ↓-spin-polarized (blue) channel of the inner $\nu = +2$ QH state carries only "cold" carriers as defined by the edges of the spin filtering $\nu = +1$ QH state and the direction of the B field. On the right-hand side of the device [blue box in Fig. 1(a)], spin detection is achieved via a reciprocal process. Here the voltmeter probes **A** and **B** are connected to the inner and outer $\nu = +2$ regions to detect a nonlocal signal V_{nl}. Since the central $\nu = 0$ region does not carry a charge current, a finite V_{nl} indicates the presence of pure spin current through the graphene antiferromagnetic insulator (AFMI) [16]. Specifically, it directly probes the chemical potential imbalances ($V_A − V_B$), and the sign of the detected signal indicates a dominant spin polarization: the voltage probe **A** detects an excess of the ↑-spin and **B** detects an excess of the ↓-spin angular momentum. Since in this experiment we also change orientation of the magnetic field, we choose an assignment of the spin directions shown in Fig. 1(b) as a reference for the rest of the data shown in this study, i.e., we define spin up and spin down as out of page and into page, respectively. We define the magnetic field and charge-carrier spin directions with respect to Fig. 1(b), assuming that electronlike states misalign their spin with the magnetic field thus occupying a higher-energy broken symmetry state, while holelike QH states align their spin with the magnetic field thus acquiring an opposite to electrons spin polarization [21].

III. MAGNETORESISTANCE DATA

An essential ingredient for such spin-signal detection is a development of QH plateaus in transverse magnetoresistance data R_{xy}, which indicates a formation of
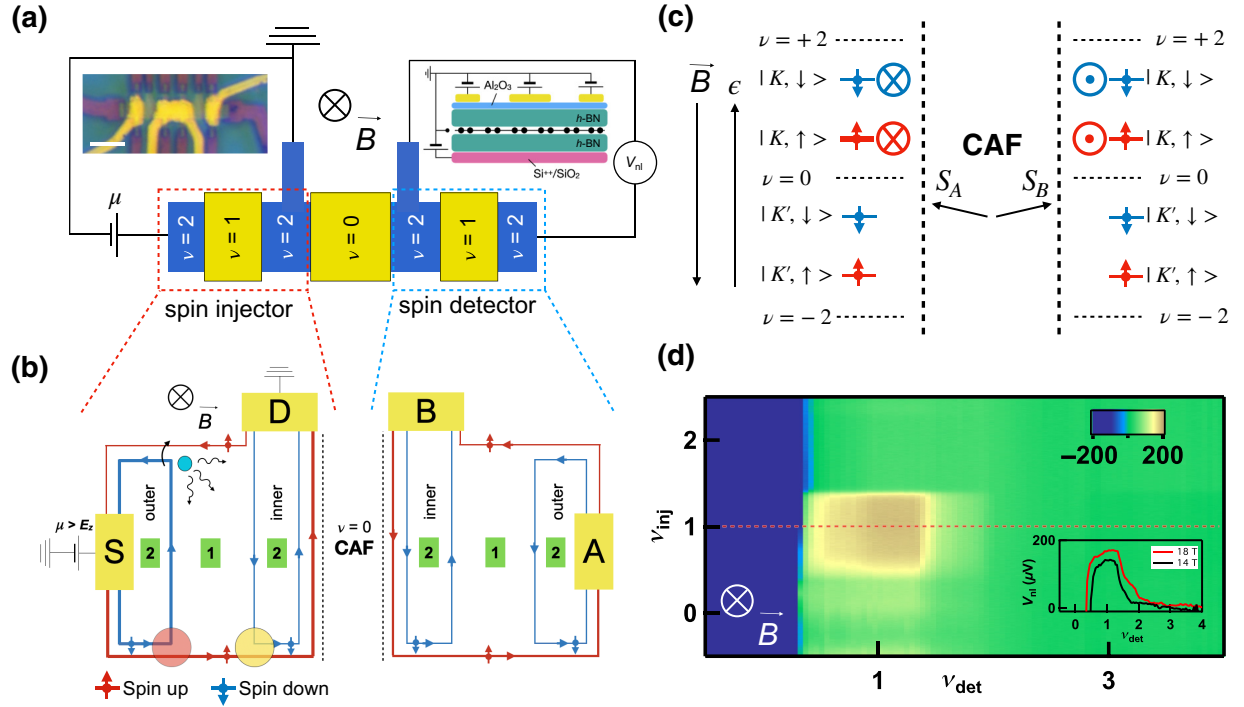
FIG. 1. Spin-transport detection. (a) All-graphene electric circuit schematics. Blue regions are "bare" back gated. Yellow regions are gated independently with both bottom and top gates. Dashed red- (blue-) line boxes show injection (detection) region, respectively. The left inset demonstrates an optical micrograph of a typical device (scale bar is 5 μm). The right inset shows the heterostructure profile that consists of an encapsulated MLG layer and three metal top gates. (b) QH edge states inside the spin-injection and spin-detection regions. Solid red (blue) lines demonstrate QH-state edge channels with ↑(↓)-spin polarization. Thicker (thinner) lines refer to the "hot" ("cold") edges, that carry high (low) chemical potential, respectively. The direction of the magnetic field is chosen to be into the plane of the figure leading to the counterclockwise propagating electronlike edge channels. (c) Detailed configuration of zeroth LL states near the graphene easy-plane AFMI $\nu = 0$ region. CAF state is sandwiched between the two inner QH states at fillings $\nu = +2$ that host two co-propagating edge channels (marked by circles) with spin-angular-momentum imbalance indicated by a thicker ↑-polarized red line. (d) Experimental measurements of the nonlocal signal (in μV) at $B = 18$ T and $T = 1.8$ K. The inset in the right lower corner shows line traces at $B = 18$ T (red) and $B = 14$ T (black) taken along the red dashed line.

topological edge currents in the sample edges. For this purpose, we perform the R_{xx} and R_{xy} measurements shown in Fig. 2. Figures 2(a) and 2(b) demonstrate contour plots that clearly exhibit Landau fan diagrams for longitudinal and transverse resistances, respectively. Figures 2(c) and 2(d) show the linecuts taken at $B = 18$ T and -18 T. Here, we observe well-developed QH plateaus with R_{xy} taking discrete values at h/e^2, $h/2e^2$, $h/3e^2 \ldots$, where h is Plank's constant and e is elementary change, while R_{xx} vanishes, overall signaling QH edge channel formations.

We precisely identify positions of different QH plateaus on the V_{TG}–V_{BG} map. For this purpose we measure R_{xy} as a function of top-gate and back-gate voltages at constant $B = 18$ T (Fig. 3). A set of stripes of the same quantization numbers emerge for finite ranges of the gate voltages. The stripes that do not exhibit dependence on the top-gate voltage (horizontal dashed lines) correspond to a single-gate like geometry, where only the back gate remains effective. These back-gate values are used to tune the Fermi level within the ¨bare¨ regions of the sample. The stripes that

exhibit dependence on the top-gate voltage, in contrast, correspond to the regions where both gates are effective and these values are utilized to tune the Fermi level in the top-gated regions of the sample.

IV. BIAS DEPENDENCE OF SPIN-TRANSPORT SIGNAL

Electrons residing on graphene sublattices **A** and **B** in the CAF state acquire oppositely directed spins with a small out-of-plane canting caused by the Zeeman effect [Fig. 1(c)] [21]. When impinging upon the CAF, the incident spin current on the left side of the CAF favors the formation of the spiral Neél texture that carries spin current collectively [11]. During the measurements, the Fermi levels of the bare ($\nu = +2$) and central top-gated ($\nu = 0$) regions are fixed, and the filling factors under the side top gates inside the injection and detection regions (ν_{inj} and ν_{det}, respectively) are varied. Typical data is shown in Fig. 1(d), which demonstrates V_{nl} versus ν_{inj} and ν_{det}
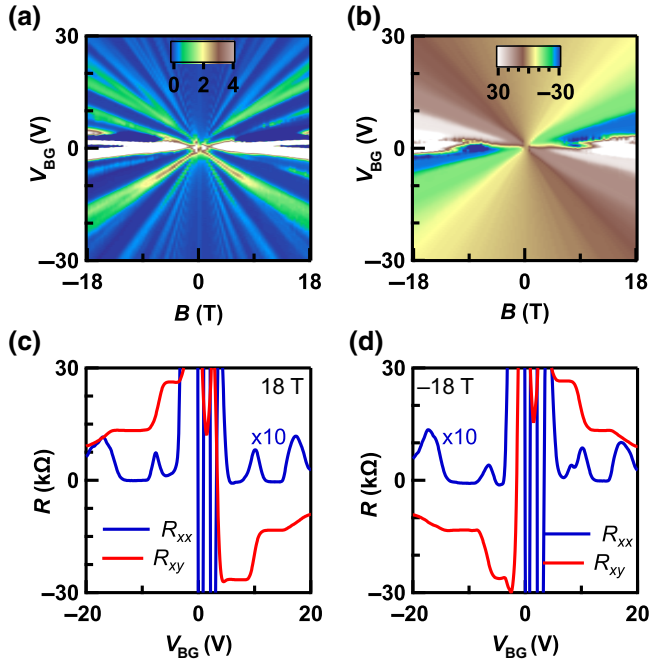
(a) **(b)** **(c)** **(d)**

FIG. 2. Magnetoresistance measurements and the QH effect in the graphene monolayer device. (a), (b) Contour plots of R_{xx} and R_{xy} (in kΩ) measured as a function of back-gate voltage and magnetic field ($V_{TG} = 0$ V) in the central region of the device using a Hall-bar geometry. (c), (d) R_{xx} and R_{xy} versus V_{BG} taken at 18 T and -18 T, respectively. Linecuts demonstrate the high-quality QH effect with well-developed plateaus within the zeroth LL of graphene. $T = 0.5$ K.
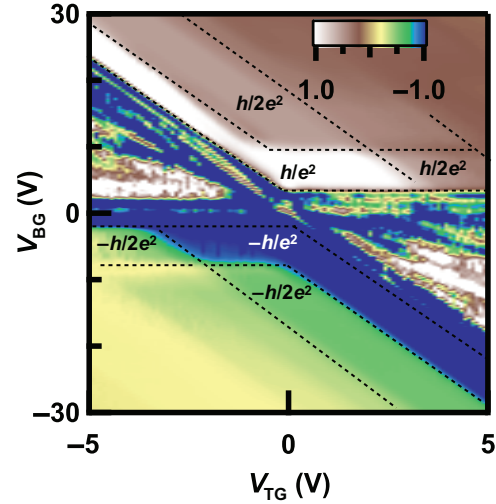

FIG. 3. Magnetoresistance measurements of R_{xy} (in units of h/e^2) at constant $B = 18$ T. This data is used to identify proper positions of QH plateaus on the gate-voltage map, which is further used to tune the "bare" and top-gated regions into QH states of interest.

at $B = 18$ T and $T = 1.8$ K. We observe a large non-local response $V_{nl} \sim 170$ μV (see inset V_{nl} versus ν_{det}), only when both the injection and the detection top-gated regions' Fermi levels are set at $\nu = +1$ QH states. The details of this experiment are given elsewhere [16].

We now turn our attention to tuning the observed non-local signal via available experimental knobs. Since the spin-angular-momentum imbalance between ↑- and ↓-spin-polarized edge channels is vital for spin-current propagation, we choose to explore V_{nl} versus ν_{det} and ν_{inj} under a reversed S-D bias voltage. Figure 4(a) shows nonlocal measurements at $\mu < -E_z$ ($V_{bias} = -65$ mV). We observe a clear suppression of the nonlocal signal. The nonlocal signal demonstrates a weakly negative response $V_{nl} \sim -30$ μV when both $\nu_{det} = \nu_{inj} = +1$ (see inset). We further observe the asymmetry in V_{nl} by varying the S-D bias in Fig. 4(c). Here we fix $\nu_{inj} = +1$ and measure V_{nl} as a function of ν_{det} and V_{bias}. Our data demonstrates a shift of maximized nonlocal voltage for the negative V_{bias} compared to the positive V_{bias} [yellow stripes in Fig. 4(d)]. The maximum signal (V_{nl}) under positive bias occurs at $V_{bias} = 65$ mV ($\mu > E_z$) with magnitude $V_{nl} \sim 170$ μV, while the maximum signal under negative bias occurs at a substantially larger $-V_{bias} = 240$ mV ($\mu < -E_z$), with a

smaller magnitude signal, $V_{nl} \sim 110$ μV. Suppression of the nonlocal signal is inconsistent with the scenario when the interchannel scattering between the adjacent QH edge states is neglected.

We explain these observations by examining the edge-state configuration shown in Fig. 4(b). At negative bias, the hot edge that carries more spin-polarized charge current is propagating from **D** to **S** and only residual QH current propagates further through the ↑-spin channel. The hot ↑-spin-polarized QH edge state does not undergo a spin-filtering process through the $\nu_{inj} = +1$ QH state region as it equilibrates on the source electrode, and the spin-angular-momentum imbalance on the edge of CAF is dominated by the hot ↓-spin channel inside the inner $\nu = +2$ in the spin-injector region. We note that the biases applied to our devices are larger than the Zeeman energy splitting between the ↑- and ↓-spin-polarized edge channels ($|\mu| = |eV_{bias}| > E_z \sim 2.08$ meV at 18 T). This implies that the electrons in the hot edge acquire enough energy to overcome the energetic barrier defined by the spatial displacement of the edge channels' wave functions [36,37] and flip their spins at localized "hotspots" [light-blue circles in Figs. 1(b) and 4(b), respectively]. This allows for an extra angular momentum to propagate inside the bulk of $\nu = +1$ QH state [10,11,38–42]. We note that only ↓-spin-polarized angular momentum can propagate into a ↑-spin-polarized bulk. Furthermore, an extra angular momentum can be absorbed by the QH edges on the opposite corners of $\nu = +1$ QH state resulting in a spin flip via a reverse process. It has been previously demonstrated that such spin transfer is mediated by magnons [17]. Therefore, the location at which the magnons are launched due to the
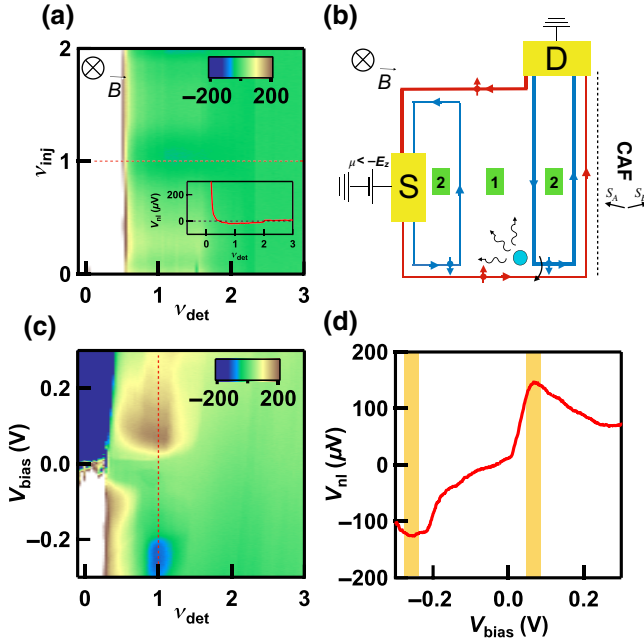
FIG. 4. Demonstration of spin-current switch using a reversed bias circuit. (a) V_{nl} (in μV) under reversed bias $V_{bias} = -65$ mV ($\mu < -E_z$) at $T = 0.5$ K. Inset shows a linecut taken along the red dashed line. Note a significantly suppressed nonlocal signal around $\nu_{det} = +1$. (b) Schematic image of QH states' configuration under the inverted voltage bias. Note the change in "hot" and "cold" edge-state configuration compared to Fig. 1(b). The light-blue circle indicates magnons launched into the ferromagnetic bulk. (c) V_{nl} (in μV) as a function of ν_{det} and V_{bias-} at a fixed $\nu_{inj} = +1$. (d) V_{nl} versus V_{bias} taken along the $\nu_{det} = +1$ in (c). Yellow stripes indicate maximized V_{nl}. We observe a significant asymmetry in the acquired data.

FIG. 5. Demonstration of the spin-current switch using an oppositely directed magnetic field. (a) V_{nl} (in μV) under the inverted $B = -18$ T at $T = 0.5$ K. Inset shows a linecut taken along the red dashed line. (b), (c) Schematic images that explain QH edge-state configuration under the inverted magnetic fields inside the spin-injection (b) and spin-detection (c) regions. Nonlocal signal quenching is attributed to the absence of the spin angular momentum on the edge of the CAF state since both copropagating channels in the inner $\nu = +2$ region originate from the same "cold" electrode D.

interchannel scattering process becomes relevant. For positive V_{bias} [Fig. 1(b)] it happens farther from the edge of the CAF state, meaning the effect of the interchannel scattering is insignificant. In the case of negative V_{bias} [Fig. 4(b)], the loss of spin angular momentum happens closer to the injection site, thus suggesting a larger loss of the momenta at the edge of the CAF and leading to a smaller nonlocal response.

Edge-channel equilibration plays a role in the studied devices. We would like to highlight that n–n'–n (p–p'–p) junctions in the injector and the detector regions have lateral dimensions smaller (approximately 1 μm) than expected for partial or full equilibration between graphene QH-state wave functions [43]. Therefore, the spin channels in the inner and the outer $\nu = +2$ regions are not equilibrated and experience a spin-flip process assisted by the angular precession of the ferromagnetic bulk only at the designated spots (marked light-blue circles). In addition to Gilbert damping in AFMIs [12], the described mechanisms of angular-momentum loss have a dramatic effect on the efficiency of the spin transport. Taking the ratio
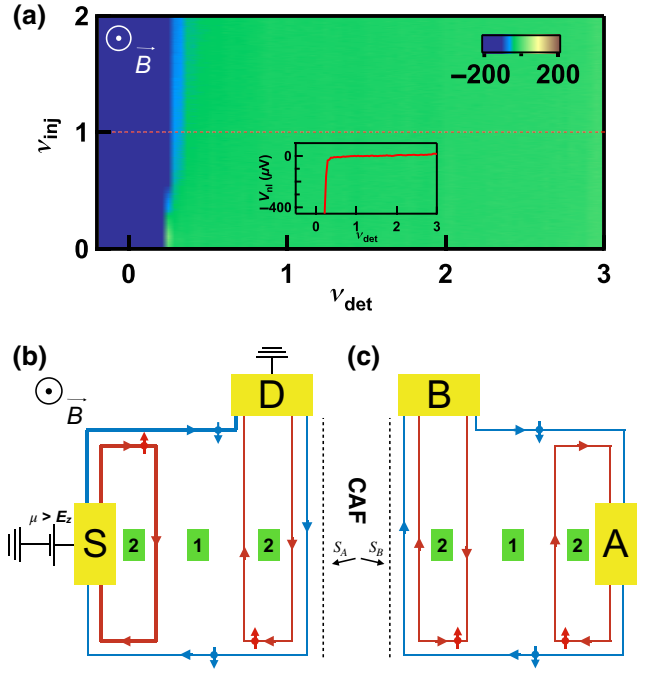
$V_{nl}/V_{bias} \sim 10^{-3}$, our approximate estimation yields [16, 44] a spin-transport efficiency parameter approximately 10^{-2}–10^{-4}, which is in a good agreement with previous studies in AFMIs [45–47].

V. SWITCHING OFF THE SPIN CURRENT IN GRAPHENE AFMIS

Next, we manipulate the spin current by utilizing a B field of the opposite direction. Figure 5(a) shows V_{nl} versus ν_{det} and ν_{inj} at reversed magnetic field $B = -18$ T at $T = 0.5$ K ($V_{bias} = 65$ mV). Interestingly, the nonlocal signal is completely quenched $V_{nl} \sim 0$ μV indicating that no spin current propagates through AFMI [Fig. 5(a)]. We attribute this observation to the equilibration of spin angular momentum in the ↑-spin- and ↓-spin-polarized edge channels in the inner $\nu = +2$ on the left edge of the CAF. Under reversal of the magnetic field, the QH-edge channels change their direction of propagation from counterclockwise (Figs. 1 and 4) to clockwise [Fig. 5(b)]. In this case, both co-propagating inner $\nu = +2$ "cold" edge channels originate from the drain electrode avoiding spin-selective
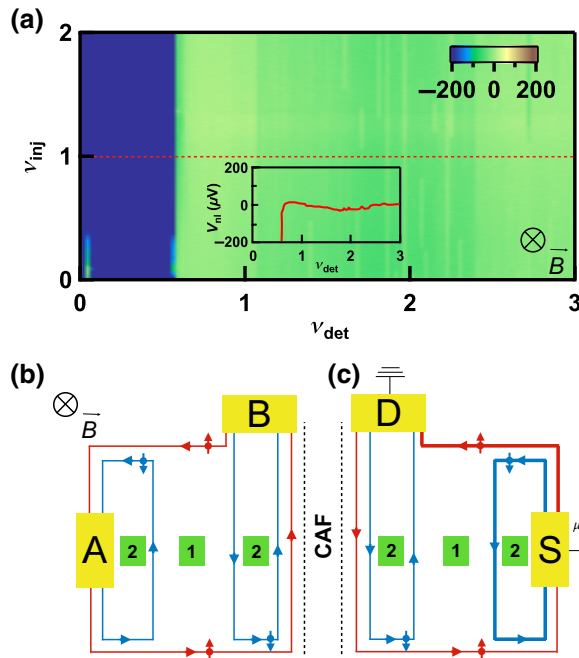
FIG. 6.　Effect of the reversed spin injector and detector sides. (a) Measurements of the nonlocal response under inverted spin injector and detector sides of the device in contrast to that shown in Fig. 1(b). $B = 18$ T and $T = 0.5$ K. Inset shows a line trace taken along the red dashed line. (b), (c) Schematic images of the QH-state configuration inside the spin-detector (b) and spin-injector (c) regions.

FIG. 7.　Utilizing holelike LLs for spin-current detection. (a) Hole-side nonlocal measurements (in μV) demonstrate strong spin-current response around $\nu_{det} = \nu_{inj} = -1$. Inset shows a line trace taken along the red dashed line. (b) Schematic images of the edge states' configuration in the injection and (c) the detection regions in the case of measurements shown in (a). Note that here we detect the oppositely directed spin current compared to Fig. 1(d) due to the higher chemical potential of the ↓-spin channel in the inner $\nu = -2$ region. Dotted red and blue lines indicate holelike QH edge states with ↑- and ↓-spin polarizations, respectively.

$\nu = +1$ QH state. This results in the absence of net spin on the edge of $\nu = 0$ AFMI and, therefore, the absence of nonlocal response in the detection region of the device.

A similar effect of spin-current shut-off can be achieved by switching sides of the detector and the injector regions in the original configuration of Figs. 1 and 4 (see Fig. 6). Just like in the case of Fig. 5, we observe a clear quenching of spin transport. Similarly to the case of reversed magnetic field polarity, spin angular momentum is absent on the edge of CAF as the "cold" charge carriers do not undergo spin-filtering process. They emanate from the drain electrode maintaining no spin-angular-momentum imbalance on the edge of CAF state (now on the right-hand side of CAF state).

VI. UTILIZING HOLELIKE QH STATES TO MANIPULATE SPIN TRANPORT

Finally, taking advantage of the ambipolar charge transport in graphene, we examine spin transport using holelike QH states. Figure 7(a) demonstrates an example of a measurement performed using a holelike set of QH states at LLs with fillings $\nu = -2/-1/-2/0/-2/-1/-2$. The spin-filtering and transport mechanisms in the case of holelike states are identical to the former case of electronlike states.
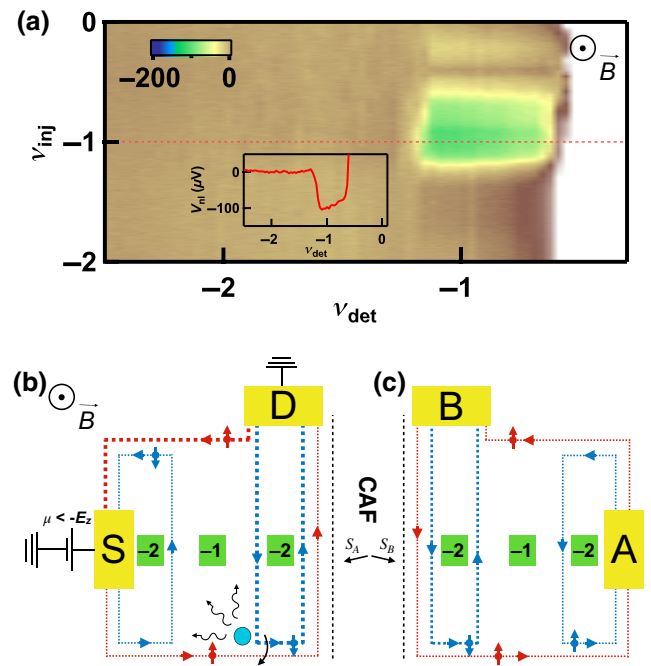
Similar to $\nu = +1$, the QH state at $\nu = -1$ is a ferromagnetic insulator with one spin-polarized edge channel. In order to detect spin-current signals, we have to account for the sign of quasiparticle charges in addition to the magnetic field and bias directions. A schematic image shown in Fig. 7(b) illustrates the configuration of the edge states in the injection region for the experiment shown in Fig. 7(a). Holelike quasiparticles move counterclockwise undergoing spin selection through a $\nu = -1$ QH state resulting in the spin chemical potential imbalance at the edge of the graphene AFMI similar to Fig. 1(c). In addition, we change the bias sign $V_{bias} = -65$ mV ($\mu < -E_z$) to select the ↓-spin-polarized edge channel. As a result, we observe a strong nonlocal signal $V_{nl} \sim -100$ μV [Fig. 4(a)] when $\nu_{det} = \nu_{inj} = -1$. In the case of a reversed magnetic field polarity for the holelike QH states (Fig. 8), we expectedly observe a disappearance of the nonlocal signal owning to the spin-angular-momentum absence on the edge of the CAF state. This scenario is very similar to the case of the electronlike QH states shown in Fig. 5, where the spin-filtering processes are shut down and the edge channels on
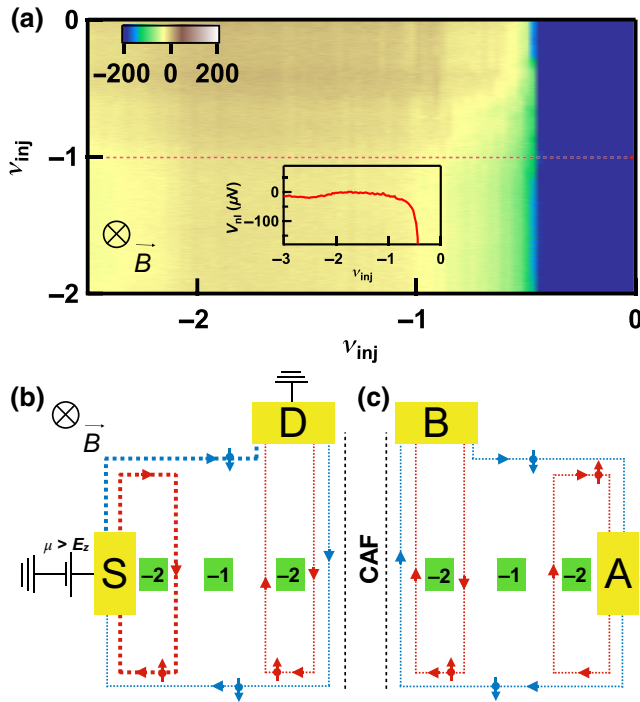
FIG. 8.   Nonlocal measurements for the hole-type carriers at $B = 18$ T. (a) Measurements of the nonlocal response for the hole-type carriers in Fig. 1(d). Inset shows a line trace taken along the red dashed line. (b), (c) Schematic images of the QH-state configuration inside the spin-injector (b) and spin-detector (c) regions. The absence of the nonlocal response is explained by the reversed current direction in the edge channels of the QH states for the hole-type carriers compared to electronlike [Fig. 1(d)], which leads to the absence of spin angular momentum on the left edge of CAF in the injector region side (b).

the left-hand side of the graphene AFMI originate from the **D** electrode.

VII. CONCLUSIONS

To conclude, our results demonstrate a high sensitivity of the pure spin transport through a $\nu = 0$ graphene AFMI to various experimental parameters. The "*on*" and "*off*" states of the nonlocal response are dependent on the edge-state propagation direction that can be tuned by a number of direction-sensitive parameters, such as magnetic field orientation, polarity of biasing voltage, and chirality of the charge quasiparticles. These observations demonstrate independent manipulation of spin current that may be carried by either electrons or holes, and further expands graphene as a versatile platform to study antiferromagnetic and ferromagnetic spintronics. Further experiments would be required to establish length, width, mobility dependencies of nonlocal signal responses. A number of additional experiments will be required to achieve a nearly dissipationless spin transport in practical magnetic materials for information processing and storage applications.

SIGN CONVENTION

We choose to assign the spins in the spin-resolved edge channels as follows: we opt to define ↑- (↓-) spin irection as out of (into the) page. Magnetic field directions are chosen in an identical way: up (down) B field is chosen out of (into the) page. We choose the excitation bias values to match chemical potential signs for both electrons and holes.

[1] V. Baltz, A. Manchon, M. Tsoi, T. Moriyama, T. Ono, and Y. Tserkovnyak, Antiferromagnetic spintronics, Rev. Mod. Phys. **90**, 15005 (2018).

[2] T. Jungwirth, X. Marti, P. Wadley, and J. Wunderlich, Antiferromagnetic spintronics, Nat. Nanotechnol. **11**, 231 (2016).

[3] P. Wadley, B Howells, J Železný, C Andrews, V Hills, R P Campion, V Novák, K Olejník, F Maccherozzi, S S Dhesi, *et al.*, Electrical switching of an antiferromagnet, Science **351**, 587 (2016).

[4] A. S. Núñez, R. A. Duine, P. Haney, and A. H. MacDonald, Theory of spin torques and giant magnetoresistance in antiferromagnetic metals, Phys. Rev. B **73**, 214426 (2006).

[5] H. Wang, C. Du, P. C. Hammel, and F. Yang, Antiferromagnonic Spin Transport from $Y_3Fe_5O_{12}$ into NiO, Phys. Rev. Lett. **113**, 97202 (2014).

[6] H. Wang, C. Du, P. C. Hammel, and F. Yang, Spin transport in antiferromagnetic insulators mediated by magnetic correlations, Phys. Rev. B **91**, 220410 (2015).

[7] C. Hahn, G. de Loubens, V. V. Naletov, J. Ben Youssef, O. Klein, and M. Viret, Conduction of spin currents through insulating antiferromagnetic oxides, Europhys. Lett. **108**, 57005 (2014).

[8] T. Moriyama, S. Takei, M. Nagata, Y. Yoshimura, N. Matsuzaki, T. Terashima, Y. Tserkovnyak, and T. Ono,

Anti-damping spin transfer torque through epitaxial nickel oxide, Appl. Phys. Lett. **106,** 162406 (2015).

[9] M. Tsoi, A. G. M. Jansen, J. Bass, W.-C. Chiang, V. Tsoi, and P. Wyder, Generation and detection of phase-coherent current-driven magnons in magnetic multilayers, Nature **406,** 46 (2000).

[10] A. V. Chumak, V. I. Vasyuchka, A. A. Serga, and B. Hillebrands, Magnon spintronics, Nat. Phys. **11,** 453 (2015).

[11] S. Takei, A. Yacoby, B. I. Halperin, and Y. Tserkovnyak, Spin Superfluidity in the $\nu = 0$ Quantum Hall State of Graphene, Phys. Rev. Lett. **116,** 216801 (2016).

[12] S. Takei, T. Moriyama, T. Ono, and Y. Tserkovnyak, Antiferromagnet-mediated spin transfer between a metal and a ferromagnet, Phys. Rev. B **92,** 20409 (2015).

[13] S. Takei, B. I. Halperin, A. Yacoby, and Y. Tserkovnyak, Superfluid spin transport through antiferromagnetic insulators, Phys. Rev. B **90,** 94408 (2014).

[14] J. König, M. C. Bønsager, and A. H. MacDonald, Dissipationless Spin Transport in Thin Film Ferromagnets, Phys. Rev. Lett. **87,** 187202 (2001).

[15] A. Qaiumzadeh, H. Skarsvåg, C. Holmqvist, and A. Brataas, Spin Superfluidity in Biaxial Antiferromagnetic Insulators, Phys. Rev. Lett. **118,** 137201 (2017).

[16] P. Stepanov, S. Che, D. Shcherbakov, J. Yang, R. Chen, K. Thilahar, G. Voigt, M. W. Bockrath, D. Smirnov, K. Watanabe, T. Taniguchi, R. K. Lake, Y. Barlas, A. H. MacDonald, and C. N. Lau, Long-distance spin transport through a graphene quantum Hall antiferromagnet, Nat. Phys. **14,** 907 (2018).

[17] D. S. Wei, T. van der Sar, S. H. Lee, K. Watanabe, T. Taniguchi, B. I. Halperin, and A. Yacoby, Electrical generation and detection of spin waves in a quantum Hall ferromagnet, Science **362,** 229 (2018).

[18] H. Zhou, H. Polshyn, T. Taniguchi, K. Watanabe, and A. F. Young, Solids of quantum Hall skyrmions in graphene, Nat. Phys. **16,** 154 (2020).

[19] H. Fu, K. Huang, K. Watanabe, T. Taniguchi, and J. Zhu, Gapless Spin Wave Transport through a Quantum Canted Antiferromagnet, Phys. Rev. X **11,** 21012 (2021).

[20] A. F. Young, J. D. Sanchez-Yamagishi, B. Hunt, S. H. Choi, K. Watanabe, T. Taniguchi, R. C. Ashoori, and P. Jarillo-Herrero, Tunable symmetry breaking and helical edge transport in a graphene quantum spin Hall state, Nature **505,** 528 (2014).

[21] M. Kharitonov, Edge excitations of the canted antiferromagnetic phase of the $\nu = 0$ quantum Hall state in graphene: A simplified analysis, Phys. Rev. B **86,** 75450 (2012).

[22] A. J. M. Giesbers, L. A. Ponomarenko, K. S. Novoselov, A. K. Geim, M. I. Katsnelson, J. C. Maan, and U. Zeitler, Gap opening in the zeroth Landau level of graphene, Phys. Rev. B **80,** 201403 (2009).

[23] Y. Zhao, P. Cadden-Zimansky, Z. Jiang, and P. Kim, Symmetry Breaking in the Zero-Energy Landau Level in Bilayer Graphene, Phys. Rev. Lett. **104,** 66801 (2010).

[24] A. F. Young, C. R. Dean, L. Wang, H. Ren, P. Cadden-Zimansky, K. Watanabe, T. Taniguchi, J. Hone, K. L. Shepard, and P. Kim, Spin and valley quantum Hall ferromagnetism in graphene, Nat. Phys. **8,** 550 (2012).

[25] Q. Sun and X. C. Xie, Spin-polarized $\nu = 0$ state of graphene: A spin superconductor, Phys. Rev. B **87,** 245427 (2013).

[26] K. Nomura and A. H. MacDonald, Quantum Hall Ferromagnetism in Graphene, Phys. Rev. Lett. **96,** 256602 (2006).

[27] J. Alicea and M. P. A. Fisher, Graphene integer quantum Hall effect in the ferromagnetic and paramagnetic regimes, Phys. Rev. B **74,** 75422 (2006).

[28] D. A. Abanin, K. S. Novoselov, U. Zeitler, P. A. Lee, A. K. Geim, and L. S. Levitov, Dissipative Quantum Hall Effect in Graphene near the Dirac Point, Phys. Rev. Lett. **98,** 196806 (2007).

[29] M. O. Goerbig, R. Moessner, and B. Douçot, Electron interactions in graphene in a strong magnetic field, Phys. Rev. B **74,** 161407 (2006).

[30] S. Kim, K. Lee, and E. Tutuc, Spin-Polarized to Valley-Polarized Transition in Graphene Bilayers at $\nu = 0$ in High Magnetic Fields, Phys. Rev. Lett. **107,** 16803 (2011).

[31] Z. Jiang, Y. Zhang, H. L. Stormer, and P. Kim, Quantum Hall States Near the Charge-Neutral Dirac Point in Graphene, Phys. Rev. Lett. **99,** 106802 (2007).

[32] J. G. Checkelsky, L. Li, and N. P. Ong, Divergent Resistance at the Dirac Point in Graphene: Evidence for a Transition in a High Magnetic Field, Phys. Rev. B **79,** 115434 (2009).

[33] J. G. Checkelsky, L. Li, and N. P. Ong, Zero-Energy State in Graphene in a High Magnetic Field, Phys. Rev. Lett. **100,** 206801 (2008).

[34] M. Kharitonov, Phase diagram for the $\nu = 0$ quantum Hall state in monolayer graphene, Phys. Rev. B **85,** 155439 (2012).

[35] D. A. Abanin, P. A. Lee, and L. S. Levitov, Spin-Filtered Edge States and Quantum Hall Effect in Graphene, Phys. Rev. Lett. **96,** 176803 (2006).

[36] D. B. Chklovskii, B. I. Shklovskii, and L. I. Glazman, Electrostatics of edge channels, Phys. Rev. B **46,** 4026 (1992).

[37] S. Komiyama, H. Hirai, M. Ohsawa, Y. Matsuda, S. Sasa, and T. Fujii, Inter-edge-state scattering and nonlinear effects in a two-dimensional electron gas at high magnetic fields, Phys. Rev. B **45,** 11085 (1992).

[38] S. M. Girvin, in *Aspects Topologiques de La Physique En Basse Dimension. Topological Aspects of Low Dimensional Systems*, edited by A. Comtet, T. Jolicœur, S. Ouvry, F. David (Springer Berlin Heidelberg, Berlin, Heidelberg, 1999), pp. 53–175.

[39] A. G. Green and N. R. Cooper, Dissipative transport in quantum Hall ferromagnets by spin-wave scattering, Phys. Rev. B **65,** 125329 (2002).

[40] Y. Kajiwara, K. Harii, S. Takahashi, J. Ohe, K. Uchida, M. Mizuguchi, H. Umezawa, H. Kawai, K. Ando, K. Takanashi, S. Maekawa, and E. Saitoh, Transmission of electrical signals by spin-wave interconversion in a magnetic insulator, Nature **464,** 262 (2010).

[41] L. J. Cornelissen, J. Liu, R. A. Duine, J. Ben Youssef, and B. J. van Wees, Long-distance transport of magnon spin information in a magnetic insulator at room temperature, Nat. Phys. **11,** 1022 (2015).

[42] D. Wesenberg, T. Liu, D. Balzar, M. Wu, and B. L. Zink, Long-distance spin transport in a disordered magnetic insulator, Nat. Phys. **13**, 987 (2017).

[43] F. Amet, J. R. Williams, K. Watanabe, T. Taniguchi, and D. Goldhaber-Gordon, Selective Equilibration of Spin-Polarized Quantum Hall Edge States in Graphene, Phys. Rev. Lett. **112**, 196601 (2014).

[44] H. Chen, A. D. Kent, A. H. MacDonald, and I. Sodemann, Nonlocal transport mediated by spin supercurrents, Phys. Rev. B **90**, 220401 (2014).

[45] Y. Zhao, Q. Song, S.-H. Yang, T. Su, W. Yuan, S. S. P. Parkin, J. Shi, and W. Han, Experimental investigation of temperature-dependent Gilbert damping in permalloy thin films, Sci. Rep. **6**, 22890 (2016).

[46] Ø Johansen and J. Linder, Current driven spin–orbit torque oscillator: Ferromagnetic and antiferromagnetic coupling, Sci. Rep. **6**, 33845 (2016).

[47] T. H. Kim, P. Grünberg, S. H. Han, and B. Cho, Ultrafast spin dynamics and switching via spin transfer torque in antiferromagnets with weak ferromagnetism, Sci. Rep. **6**, 35077 (2016).